Tribology International 183 (2023) 108356

Contents lists available at ScienceDirect

Tribology International

journal homepage: www.elsevier.com/locate/triboint

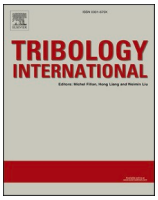

Experimental and theoretical study on the dynamic stiffness of circular oil hydrostatic shallow recess thrust bearings

Fabian A. Tripkewitz [a,b,*], Tomáš Lazák [c], Matthias Fritz [a], Eduard Stach [c], Matthias Weigold [b], Matěj Sulitka [c]

[a] KERN Microtechnik GmbH, Olympiastraße 2, 82438 Eschenlohe, Germany
[b] Technical University Darmstadt, Institute of Production Management, Technology and Machine Tools (PTW), Otto-Berndt-Straße 2, 64287 Darmstadt, Germany
[c] Czech Technical University in Prague, Faculty of Mechanical Engineering, Department of Production Machines and Equipment, RCMT, Horská 3, 128 00 Prague, Czech Republic

ARTICLE INFO

Keywords:
Hydrostatic
Thrust bearing
Dynamic
Shallow recess

ABSTRACT

The dynamic stiffness of traditional (deep recess) hydrostatic bearings decreases due to the fluid compressibility between the bearing and a compensation device, e.g., a capillary. Shallow recess bearings, on the other hand, reduce the influence of fluid compressibility on dynamic stiffness through a reduced compressible volume and inherent stiffness. This article outlines a theoretical and experimental study of the dynamic stiffness of oil hydrostatic shallow recess thrust bearings without external compensation devices and in combination with external capillaries. The measurements performed in the study validate the theoretical models and the potential to increase dynamic stiffness. In addition, analytical solutions are proposed for the stiffness and damping of a circular shallow recess thrust bearing.

1. Introduction

Precision machine tools depend on a balanced combination of damping and stiffness [1]. Hydrostatic (HS) bearings are a convenient tool to meet these requirements [2]. However, most hydrostatic applications use pockets with deep recesses and external compensation devices [3]. Since the recess is several orders of magnitude above the film thickness, its hydraulic resistance is negligible. Previous studies have dealt with both the static [3] and dynamic [4,5] behaviour of deep recess HS bearings. A disadvantage of this bearing concept is that excessive compressibility can result in increased dynamic compliance [6]. C. R. Adams developed a different bearing concept in 1958 using a shallow recess [7]. In this concept, the recess depth is of the same magnitude as the film thickness, so the pressure drop is no longer neglectable [8]. As a result, this bearing type does not require external components, significantly reducing the compressible volume. The static behaviour of shallow recess (SR) bearings is well known [8,9]. Although an additional external capillary (CAP) is not required, it can increase static stiffness [10]. Furthermore, a single shallow recess pocket can support eccentric loads [11], which externally compensated deep recess bearings are not capable of [12]. No further work exists on the dynamic behaviour of oil hydrostatic shallow recess thrust bearings with or without an external capillary.

Due to the inherent stiffness and reduced compressible volume compared to deep recess bearings, SR bearings offer the potential to have superior dynamic stiffness. This article presents a general model for the dynamic behaviour of SR bearings, which can also consider the influence of an additional external capillary and the hydraulic capacity it introduces. To validate the model, we carried out experiments with circular thrust bearings with a nominal recess depth of 10 μm and film thicknesses from 5 to 20 μm with and without external compensation devices (capillaries). Here, the frequency response function (FRF) was experimentally determined up to 2 kHz at a supply pressure of 10.5 MPa. The measurements and the models show good correspondence.

2. Material and methods

2.1. Test bench

Fig. 1 shows a sectional view of the test bench. The foundation is a massive bolted steel frame (1) to ensure high static and dynamic stiffness. The pocket module (8) and the bearing plate (6) form the

* Corresponding author at: KERN Microtechnik GmbH, Olympiastraße 2, 82438 Eschenlohe, Germany.
E-mail address: fabian.tripkewitz@kern-microtechnik.com (F.A. Tripkewitz).

https://doi.org/10.1016/j.triboint.2023.108356
Received 18 December 2022; Received in revised form 16 February 2023; Accepted 19 February 2023
Available online 23 February 2023

Nomenclature

A	Area (m^2).
A_e	Effective area (m^2).
c_1	Integration constant 1(-).
c_2	Integration constant 2 (-).
C	Hydraulic capacity (m^5/N).
d_{den}	Denominator of the damping constant (m^9).
d_{num}	Numerator of the damping constant (Nsm^8).
d_{SR}	Damping constant (Ns/m).
$f_{c,RC}$	Cut-off frequency supply system (1/s).
$f_{c,sys}$	Cut-off frequency of the system (1/s).
F	Force (N).
F_d	Damping force (N).
F_{dyn}	External dynamic excitation force (N).
F_p	Force generated by the pressure profile (N).
$F_{p,1}$	Pressure introduced force – section 1 (N).
$F_{p,2}$	Pressure introduced force – section 2 (N).
$F_{sq,I}$	Squeeze force – section I (N).
$F_{sq,II}$	Squeeze force – section II (N).
h	Film Thickness (m).
h_s	Step height (m).
h_I	Film thickness – section I (m).
h_{II}	Film thickness – section II (m).
k	Stiffness (N/m).
k_{CAP}	Static stiffness of SR pocket with CAP (N/m).
k_{SR}	Static stiffness of SR pocket (N/m).
k_{TB}	Static stiffness of test bench (N/m).
K	Isothermal tangent bulk modulus (N/m^2).
m	Moving mass (kg).
n	Number of pockets (-).
p	Pressure (N/m^2).
p_0	Pressure at the pocket inlet (N/m^2).
p_1	Pressure at the step (N/m^2).
$p_{sq,I}$	Squeeze pressure – section I (N/m^2).
$p_{sq,II}$	Squeeze pressure – section II (N/m^2).
p_p	Supply pressure (N/m^2).
Q	Volume flow (m^3/s).
Q_C	Volume flow into the capacity (m^3/s).
Q_{CAP}	Volume flow through capillary (m^3/s).
Q_{sq}	Squeeze volume flow (m^3/s).
Q_{SR}	Volume flow through SR pocket (m^3/s).
Q_I	Volume flow over recess (m^3/s).
Q_{II}	Volume flow over land (m^3/s).
r	Radius (m).
r_0	Radius of the pocket inlet (m).
r_1	Radius of the step (m).
r_2	Radius of the pocket outlet (m).
R	Hydraulic resistance (Ns/m^5).
R_a	Arithmetical mean roughness value (m).
R_{CAP}	Hydraulic resistance of the capillary (Ns/m^5).
R_{SR}	Hydraulic resistance of the SR pocket (Ns/m^5).
R_z	Mean roughness depth (m).
R_I	Hydraulic resistance – section I (Ns/m^5).
R_{II}	Hydraulic resistance – section II (Ns/m^5).
t	Time (s).
T	Temperature (°C).
T_0	Fluid temperature at the bearing inlet (°C).
V	Volume of the cavity and piping after CAP (m^3).
VI	Viscosity index (-).
w	Velocity (m/s).
w_A	Velocity of the top plane (m/s).
w_B	Velocity of the bottom plane (m/s).
x	Position along x-axis (m).
z	Position along z-axis (m).
Δp_0	Pocket inlet pressure deviation (N/m^2).
μ	Dynamic viscosity (Ns/m^2).
ν	Kinematic viscosity (m^2/s).
ν_0	Kinematic viscosity at 0 °C (m^2/s).
ν_{40}	Kinematic viscosity at 40 °C (m^2/s).
ν_{100}	Kinematic viscosity at 100 °C (m^2/s).
ρ_{15}	Density at 15 °C (kg/m^3).
σ_1	Auxiliary subexpression (m^3s/kg).
σ_2	Substitution (-).
ϕ	Angular coordinate (rad).
ω_0	Natural frequency of the undamped system (1/s).

Abbreviations

CAP	Capillary.
DAQ	Data acquisition.
DR	Deep recess.
exp	Experiment.
FRF	Frequency response function.
HS	Hydrostatic.
sim	Simulation.
SR	Shallow recess.
SR+CAP	SR bearing combined with CAP.
TB	Test bench.

hydrostatic bearing unit. The pocket module has three symmetrical, independent pockets for greater tilting stiffness (see Fig. 2). Therefore, the influence of tilting effects is neglectable. The bearing plate represents the flat mating surfaces. A flexure (5) connects the bearing plate to the frame and prevents movement in the bearing plane without restricting axial or tilting motion. A capacitive sensor (7) measures the relative displacement between the bearing plate and the pocket module, respectively, the film thickness. A parallel configuration of static and dynamic force loads the bearing unit. Preloaded disk springs (3) apply the static part and a piezo actuator (2) applies the dynamic part. A force sensor (4) mounted concentrically on the bearing plate measures the resulting total force. Two versions are available for the three supply modules (10), each with a rectangular channel geometry but different hydraulic resistances. The first version is a fixed laminar-flow restrictor which throttles the hydraulic supply (height 0.156 mm, width 2 mm, length 100 mm). In this article, the fixed laminar-flow restrictor is referred to as a capillary. The second version passes the hydraulic supply directly to the bearing with negligible hydraulic resistance (height 4 mm, width 4 mm, length 15 mm). A service port (9) enables temperature and pressure measurements between each capillary and pocket. This service port and the piping between the pocket and the capillary result in a compressible volume of $V = 2871\ mm^3$. After exiting the bearing, the fluid flows back into the hydraulic circuit through a collecting groove (11).

2.2. Bearing unit

As mentioned in the previous section, the bearing unit consists of three pockets. Fig. 2 shows an overview of the two components comprising the bearing unit.

All functional surfaces have high flatness and surface roughness requirements for measuring dynamic properties at microfilm thicknesses.

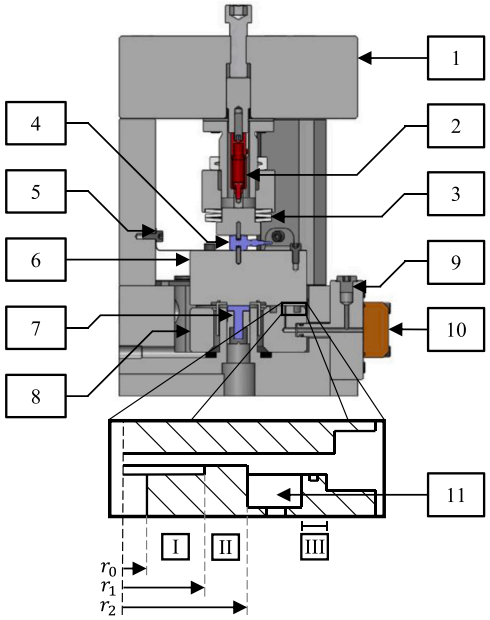

Fig. 1. Test bench cross section.

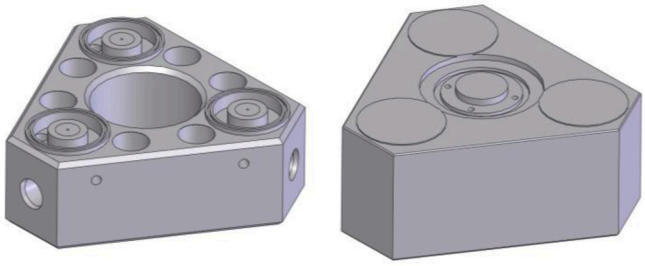

Fig. 2. Pocket module (left) and bearing plate (right).

Therefore, we first lapped both components. Subsequently, the pocket module section I (see Fig. 1) was recessed by approximately 10 µm by precision milling. This area represents the shallow recess and therefore is fundamental for the working principle. Table 1 lists the three radii, which are identical for all three circular pockets. Appendix A provides the engineering drawings of the two components.

Both components were measured in scanning mode on a ZEISS PRISMO CMM for geometric errors and a ZEISS SURFCOM 130A for surface properties, namely arithmetical mean roughness value R_a and mean roughness depth R_z. Table 2 lists all the measured properties and their values.

Since six screws hold the pocket module to the frame, preloading them can introduce distortion if the mating surfaces are uneven. Therefore, the module is glued in with Loctite 243 to compensate for any unevenness. Additionally, the screws were tightened after curing the compound. Finally, a comparative measurement in the installed state confirmed the previously measured properties listed in Table 2.

Table 1
Nominal bearing radii.

Feature	[mm]
Radius of the pocket inlet r_0	0.5
Radius of the step r_1	5
Radius of the pocket outlet r_2	8

Table 2
Measured geometric properties, dimensions and surface quality of the bearing unit.

Feature	[µm]
Bearing plate – flatness	0.5
Pocket module – flatness lands	0.4
Avg. depth Recess 1	9.4
Avg. depth Recess 2	8.9
Avg. depth Recess 3	9.1
Bearing plate – avg. Rz | Ra	1.046 | 0.151
Pocket module – land - avg. Rz | Ra	0.852 | 0.109
Pocket module – recess - avg. Rz | Ra	1.084 | 0.158
Step height h_s (for simulation)	9.1

2.3. Hydraulic supply

The nominal supply pressure p_p of 10.5 MPa and fluid temperature of 22 °C were identical for all measurements. Appendix B lists the measured values for each experiment discussed in Chapter 4.2. Table 3 shows the general physical properties of the fluid that was used.

The fluid temperature influences the squeeze damping via the dynamic viscosity µ. A temperature sensor measures the fluid inlet temperature T_o (see Fig. 1, Number 9) to consider this influence. Additionally, an external laboratory determined the fluid dynamic viscosity as a function of temperature. Eq. (1) shows the Andrade's equation fitted for a temperature range of 20–26 °C with a standard deviation of 1.8‰:

$$\mu = 0.23623e^{-0.05825T_o} \tag{1}$$

Considering pressure and temperature, the isothermal tangent bulk modulus K calculates according to Karjalainen [13]. At nominal supply pressure and fluid temperature, this leads to an isothermal bulk modulus of 1.95×10^9 N/m^2.

2.4. Data acquisition

A data acquisition (DAQ) system measures the time-critical signals related to force and displacement and temperature and pressure signals. The DAQ system consists of a CompactDAQ-9188 from National Instruments with multiple input modules. A NI-9239 records the time-critical signals with simultaneous sampling at 50 kS/s/ch and 24-bit resolution. In addition, an integrated passband filter up to 22.65 kHz prevents aliasing. The high sampling rate was selected to investigate the FRF of the test bench up to 5 kHz with the identical setup, which requires a sampling rate greater than 10 kHz. Table 4 gives an overview of the hardware.

2.5. Measuring Methodology

We assume a linear time-invariant system for the following analysis. A test signal with frequencies from 0.1 to 2000 Hz excites the bearing for the experimental determination of the dynamic stiffness. The first eigenfrequency of the test bench at 2.5 kHz limits the maximum excitation frequency. The DAQ system, with a sampling frequency of 50 kHz

Table 3
Properties of the hydraulic fluid.

Oil type	Kinematic viscosity at 0 °C ν_0	Kinematic viscosity at 40 °C ν_{40}	Kinematic viscosity at 100 °C ν_{100}	Viscosity index VI	Density at 15 °C ρ_{15}
VG 32	338 $\frac{mm^2}{s}$	32 $\frac{mm^2}{s}$	5.4 $\frac{mm^2}{s}$	99	875 $\frac{kg}{m^3}$

Table 4
DAQ hardware.

Device	Type	Amplifier	DAQ module
Force sensor	CFT/20 kN	CMC/ 20 kN	NI-9239
Displacement sensor	PISeca D – 510.051	E-852.10	NI-9239
Temperature sensor	PT 100 class A, 4 wire	-	NI-9219
Pressure sensor	WIKA PE 81.60 Model A-10	-	NI-9205
Force actuator	PI P842.20	E-617 LVZT	NI-9263

and an integrated anti-aliasing filter, satisfies the Nyquist-Shannon theorem. According to the Rayleigh Criterion, one measurement consists of a discrete number of 2^{19} samplings, resulting in a frequency resolution of 0.095 Hz and a measurement time of 10.486 s.

2.5.1. Test signals

The excitation signal consists of a multi-sine. Furthermore, the discrete number of sampling points always equals an integer multiple of the frequencies. As a result, the processing does not require any window function and no leakage occurs.

The amplitude is equal for all frequencies but with different phases, according to Schröder [14], which requires a linear equidistant spacing of the frequencies. Therefore, the frequency spectrum is divided into four logarithmically equidistant sections for efficient measurements, each subdivided with 110 linear equidistant spaced frequencies.

2.5.2. Evaluation of estimated transfer function

Using multi-sine signals enables the detection of linear and nonlinear behaviour, whereby the assumption of linear behaviour is verifiable. The coherence function, which grades the linearity of the input and output signals on a scale of zero to one, serves for evaluation purposes. A value of one indicates exact linear behaviour. The estimation of the transfer function is based on the H1 principle [15].

2.6. Test bench stiffness

To compare the measurements with the theoretical model (see Section 3), the model must also consider the influence of the test bench. For this purpose, we measured the deflection at static load without hydraulic supply and dry bearing surfaces. Fig. 3 shows the measured data. Due to the flatness errors and surface roughness (see Table 2), the contact stiffness is nonlinear at low preload (< 1.25 kN). However, constant stiffness and constant contact conditions exist from 1.25 to 4 kN. Since the hydrostatic oil film compensates for the existing unevenness, a constant stiffness of the test bench k_{TB}, independent of the preload, is assumed during the tests.

Without hydrostatic, the frequency spectrum of the test bench has no eigenfrequencies up to 2 kHz and thus has a constant stiffness and phase. Therefore, a simple spring with stiffness k_{TB} represents the test bench in the simulation.

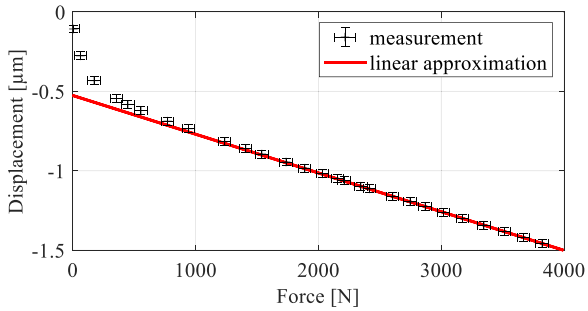

Fig. 3. Static force-displacement behaviour of the test bench.

2.7. Test procedure

The oil film thickness h has a significant influence on the dynamic stiffness. As Fig. 3 shows, any preload results in elastic deformation of the test bench, which superposes the fluid film height during the measurements. To compensate for these elastic deformations, we zeroed the displacement sensor at a preloaded of 4 kN. The high preload squeezes the fluid residues out of the mating surfaces, resulting in a defined contact. This procedure allows for a reproducible reference. However, each film height requires a different preload, which differs from 4 kN, resulting in a change in the elastic deformation at the corresponding preload. Therefore, the reading of the displacement sensor is adjusted to compensate for the elastic deformations of the test bench. This compensated film height equals the sum of the nominal fluid film height and the elastic deformation resulting from the change in preload relative to 4 kN.

The film thickness was set before each measurement. Subsequently, the test bench was tempered under the selected operating conditions for at least four hours to reach thermal equilibrium. The film thickness was then set again to compensate for thermal deformation. Finally, the frequency response function (FRF) was measured. This procedure ensured stable conditions for the measurements.

For the actual FRF measurement, the force actuator excited the system with the multi-sine and the displacement transducer measured displacement simultaneously. Each measurement represents the average of five consecutive individual measurements to increase robustness. By repeating the set of measurements twice, errors are detectable.

3. Theory

Fig. 4 shows a schematic illustration of a circular SR bearing, the nomenclature used in this article and a schematic pressure profile. The fluid enters the bearing at the inner radius r_0 with the inlet pressure p_0. From here the fluid passes the recess with a height h_I. At the step radius r_1, a step with height h_s reduces the film to thickness h_{II}. The step pressure is denoted by p_1. The step pressure p_1 drops to ambient pressure at the outer diameter r_2.

The following assumptions are made for the hydraulic fluid:

- No inertia effects.
- The hydrostatic film is incompressible.
- Compressibility between capillary and pocket.
- Constant viscosity.

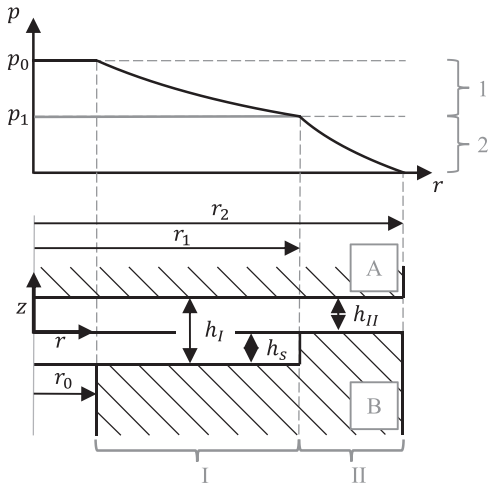

Fig. 4. Nomenclature and pressure profile of the shallow recess bearing geometry.

- No cavitation.
- No dissolved air.
- No elastic deformation of the bearing geometry.
- The dynamic displacement is relatively small (20 times less than the film thickness h_{II}).
- Neglectable hydraulic inductance of the capillary.

Furthermore, the model assumes an ideal and identical geometry for all three bearing pockets. Table 2 and Table 3 contain the corresponding values.

3.1. Mathematical model

3.1.1. Static stiffness of a shallow recess hydrostatic bearing (SR)

As mentioned previously, the SR HS bearing cavity depth is of the same magnitude as the film thickness, so the calculation must consider its hydraulic resistance. Fig. 5 shows the hydraulic schematics of the studied SR HS bearing, comprising the two annular clearances (recess and land). The hydraulic resistance of the annular clearance is well known [3]. Bassani assumes laminar flow and a small film thickness relative to the width of the annular clearance. In addition, the author neglects inlet losses into the clearance and assumes isothermal flow, respective constant viscosity. Transferring the existing approach to the SR bearings requires the assumption that the transition from the recess to the land does not influence the laminar flow or introduce transition losses. Based on these assumptions, the hydraulic resistance of the SR HS pocket R_{SR} is the sum of the hydraulic resistance of the recess R_I and land R_{II}.

$$R_I = \frac{6\mu \ln\left(\frac{r_1}{r_0}\right)}{\pi (h_{II} + h_s)^3} \tag{2}$$

$$R_{II} = \frac{6\mu \ln\left(\frac{r_2}{r_1}\right)}{\pi h_{II}^3} \tag{3}$$

With known hydraulic resistance of the SR bearing and the bearing inlet pressure, the volume flow through the SR bearing can be calculated by $Q = p_0/R_{SR}$. Based on the continuity equation $Q = Q_I = Q_{II}$, the volume flow Q is equal to the flow over the recess Q_I and the land Q_{II}. With known volume flow and hydraulic resistance of the land, the step pressure is calculated by the equation $p_1 = QR_{II}$. By substituting the volume flow, the general equation of the step pressure p_1 is obtained.

$$p_1 = p_0 \frac{R_{II}}{R_I + R_{II}} \tag{4}$$

The force introduced by the pressure over the annular clearance area of the HS bearing is also known [3]. This study divides the pressure profile into two parts, as shown in Fig. 4, denoted by 1 and 2 (not I and II). The total force F_p is the sum of the two forces, based on the pressure part 1 respective pressure part 2.

$$F_p = F_1 + F_2 \tag{5}$$

$$F_1 = \frac{\pi}{2}(p_0 - p_1)\left(\frac{r_1^2 - r_0^2}{\ln\left(\frac{r_1}{r_0}\right)}\right) \tag{6}$$

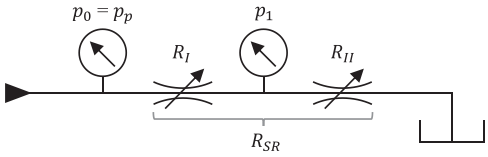

Fig. 5. Hydraulic schematics of SR HS bearing.

$$F_2 = \frac{\pi}{2} p_1 \left(\frac{r_2^2 - r_1^2}{\ln\left(\frac{r_2}{r_1}\right)}\right) \tag{7}$$

Differentiation of the force leads to the stiffness k.

$$k = -\frac{dF_p}{dz} \tag{8}$$

Combining (4),(6),(7) and (8) gives the stiffness of a SR pocket k_{SR}:

$$k_{SR} = 3\pi h_I^2 h_{II}^2 h_s p_p \frac{\left({r_1}^2\left(\ln\left(\frac{r_1}{r_0}\right) + \ln\left(\frac{r_2}{r_1}\right)\right) - {r_0}^2 \ln\left(\frac{r_2}{r_1}\right) - {r_2}^2 \ln\left(\frac{r_1}{r_0}\right)\right)}{2\left(h_{II}^3 \ln\left(\frac{r_1}{r_0}\right) + h_I^3 \ln\left(\frac{r_2}{r_1}\right)\right)^2} \tag{9}$$

3.1.2. Static stiffness of a shallow recess hydrostatic bearing compensated by a capillary (SR+CAP)

Fig. 6 shows the hydraulic schematics of the SR HS bearing controlled by a linear hydraulic resistance (capillary). It consists of a fixed resistance of the capillary R_{CAP} and a variable resistance of the recess and the land.

Based on the continuity equation $Q = Q_{CAP} = Q_I = Q_{II}$, the volume flow through the capillary Q_{CAP} equals the volume flow over the recess and the land. Combined with the pressure loss equation, the pressure at the HS pocket inlet p_0 is:

$$p_0 = p_p \frac{R_I + R_{II}}{R_{CAP} + R_I + R_{II}} = p_p \frac{R_I + R_{II}}{R} \tag{10}$$

and the pressure at the bearing step p_1 is:

$$p_1 = p_p \frac{R_{II}}{R_{CAP} + R_I + R_{II}} = p_p \frac{R_{II}}{R} \tag{11}$$

The sum of (6) and (7) is the total force F_p. The differentiation of F_p results, according to (8), in the general expression of stiffness for shallow recess bearings with external capillary k_{CAP}.

$$k_{CAP} = -\frac{\pi p_p ({r_0}^2 - {r_1}^2)}{2\ln\left(\frac{r_1}{r_0}\right)}\left(\sigma_1 (R_{CAP} + R_{II}) - \frac{3R_{II}}{h_{II}R}\right) + \frac{9\mu p_p ({r_2}^2 - {r_1}^2)}{h_{II}^4 R} - \frac{3\mu p_p ({r_2}^2 - {r_1}^2)\sigma_1}{h_{II}^3} \tag{12}$$

$$\sigma_1 = \frac{3}{R^2}\left(\frac{R_I}{h_{II} + h_s} + \frac{R_{II}}{h_{II}}\right) \tag{13}$$

3.1.3. Squeeze damping

Fig. 4 shows a schematic of the SR HS pocket. The HS pocket consists of two sections. The first section is the recess, indicated by I, whereas the second section is the land, marked by II. The model assumes that a displacement of member A in the vertical direction causes two distinct phenomena that may be separately considered.

The first phenomenon is the HS bearing effect [16]. However, this effect only serves to preserve the fluid film in the bearing and is, therefore, negligible. The second phenomenon is the squeeze effect of the liquid in the thin film. In contrast to the first effect, this causes a damping behaviour.

The Reynolds equation in polar coordinates (radius r and angle ϕ) is the governing equation for the squeeze damping of circular bearings

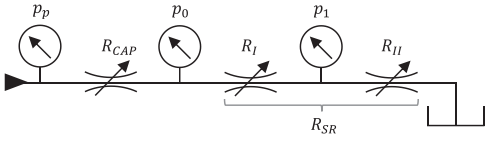

Fig. 6. Hydraulic schematics of the SR HS bearing controlled by a linear hydraulic resistance (capillary).

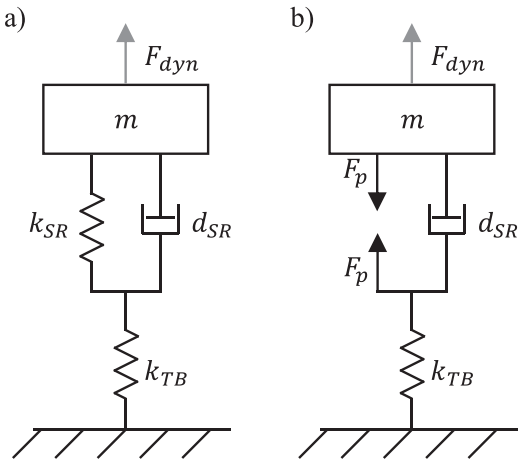

Fig. 7. Dynamic models for SR (a) and SR+CAP (b).

[17].

$$\frac{\partial}{\partial r}\left(rh^3\frac{\partial p}{\partial r}\right)+\frac{1}{r}\frac{\partial}{\partial \phi}\left(h^3\frac{\partial p}{\partial \phi}\right)=12\mu r(w_A-w_B) \tag{14}$$

The model assumes that the pressure is circularly symmetric and therefore $\partial p/\partial\phi = 0$. The bearing consists of two sections and in each section, the film thickness h is not a function of r. Member A moves downwards at the velocity w_A and member B is stationary ($w_B = 0$). Therefore, $(w_A - w_B) = -\partial h/\partial t$. Eq. (14) reduces to:

$$\frac{\partial}{\partial r}\left(rh^3\frac{\partial p}{\partial r}\right)=-12\mu r\frac{\partial h}{\partial t} \tag{15}$$

The damping constant d_{SR} results from mathematical transformations. Appendix C shows the derivation procedure in detail.

3.1.4. Dynamic pocket pressure of a shallow recess hydrostatic bearing compensated by a capillary

With a capillary, the assumption of constant supply pressure is no longer valid. Instead, the continuity equation is required to calculate the transient pocket inlet pressure $p_0(t)$. The system under consideration is the hydraulic capacity of the compressible volume V between the capillary and pocket inlet.

When the bearing is statically loaded, the volume through the capillary Q_{CAP} into the bearing must be equal to the flow out of the bearing, i.e., the flow through the recess and land Q_{SR}. In case of a dynamic loading, the squeeze flow Q_{sq} and the flow due to compressibility Q_C must also be considered to satisfy the continuity equation.

$$Q_{CAP}(t)=Q_{SR}(t)+Q_{sq}(t)+Q_C(t) \tag{16}$$

$$Q_C(t)=\frac{V}{K}\Delta\dot{p}_0(t) \tag{17}$$

$$Q_{CAP}(t)=\frac{p_p-p_0(t)}{R_{CAP}} \tag{18}$$

$$Q_{sq}(t)=\dot{h}(t)A_e \tag{19}$$

Table 5
Experimental uncertainty.

Parameter	Symbol	Unit	Uncertainty
Film thickness	h_{II}	µm	0.9
Step height	h_s	µm	0.3
Supply pressure	p_s	MPa	0.1
Fluid temperature	T	K	0.4
Dynamic viscosity	ν	‰	1.8
Hydraulic resistance of the CAP	R_{CAP}	%	4
Isothermal tangent bulk modulus	K	%	(20)

$$Q_{SR}(t)=\frac{p_0(t)}{R_{SR}(t)} \tag{20}$$

$$p_0(t)=p_0+\Delta p_0(t) \tag{21}$$

The existing inlet pressure deviation $\Delta p_0(t)$ can be calculated by numerical integration of the rate of pressure change $\Delta\dot{p}_0(t)$.

3.2. Dynamic models

Due to the inherent throttling, shallow recess bearings do not need external compensating devices, reducing the compressible fluid volume to a minimum. As a consequence, the fluid compressibility is negligible. Therefore, the derived stiffness (9) and damping (C.10) are sufficient to describe the SR bearing. The analogous mechanical replacement model consists of a spring and a damper. Fig. 7 shows the corresponding equivalent model on the left, accounting for the test bench. The equation of motion for this configuration is:

$$\frac{mnd_{SR}}{k_{TB}}\dddot{x}=\left(\frac{nk_{SR}}{k_{TB}}+1\right)\left(F_{dyn}-m\ddot{x}\right)+\frac{nd_{SR}}{k_{TB}}\dot{F}_{dyn}-nd_{SR}\dot{x}-nk_{SR}x \tag{22}$$

with the moving mass m, number of pockets n and external dynamic excitation force F_{dyn}.

An additional external compensation device significantly increases the compressible volume of the system. As a result, the fluid compressibility is not negligible. Therefore, a simple spring can no longer represent the stiffness because of the frequency dependence. However, the squeeze damping remains identical. Fig. 7 shows the corresponding equivalent model on the right, taking the test bench into account. The equation of motion for this case is as follows:

$$\frac{mnd_{SR}}{k_{TB}}\dddot{x}=-m\ddot{x}-nd_{SR}\dot{x}+\frac{nd_{SR}}{k_{TB}}\dot{F}_{dyn}+F_{dyn}+n\Delta F_p \tag{23}$$

$$\Delta F_p=F_1(\Delta p_0(t))+F_2(\Delta p_0(t)) \tag{24}$$

where F_1 and F_2 are calculated according to Eqs. (6) and (7), but with pocket inlet pressure deviation $\Delta p_0(t)$ for ΔF_p.

3.3. Simulation

Two MATLAB Simulink 2020a models were created based on the equations of motion from the previous section. The first model describes the SR bearing. The second model considers the influence of an additional capillary on the SR bearing.

4. Results and discussion

We investigated the dynamic compliance at 5, 10, 15 and 20 μm film thickness. According to Eq. (1), the fluid temperature significantly affects the viscosity. Therefore, each simulation accounts for the measured fluid temperature of the experiment. Similarly, the simulation uses the measured film thickness of the particular experiment. Each measurement represents the average of five consecutive individual measurements to increase robustness. By repeating the set of measurements twice, errors are detectable. Compliance bode plots allow for evaluating and comparing the experimental and theoretical data.

4.1. Uncertainty

4.1.1. Experimental uncertainty

The experimental uncertainty depends mainly on the individual uncertainties of seven parameters. Table 5 lists the parameters and their systematic uncertainties.

Because we could not determine the air content of the hydraulic fluid, the uncertainty of the isothermal compression modulus is only an estimation.

4.1.2. Uncertainty of the estimated transfer function

Assuming ideal behaviour, the standard deviation of the estimated amplitude and phase can be calculated based on the number of measurements and the coherence function [15].

4.2. Comparison of the simulation and measurement of a shallow recess hydrostatic bearing

Fig. 8 shows the measured and simulated dynamic compliance for the SR bearing. For comparison, the figures show the simulation results with and without considering the test bench stiffness. In addition to the simulation with nominal values, the figure shows the simulation with the experimental uncertainty, according to 4.1.1. Due to the principle of operation, the external hydraulic resistance and bulk modulus do not have any influence. To increase clarity and enable a qualitative evaluation, the uncertainty shown in the figure only includes the dominant influence, which is the uncertainty of the bearing geometry. The critical parameters of the bearing geometry are the film thickness h_{II} and the step height h_s.

Simulations and measurements show minimal deviation, especially at medium film thicknesses. At 5 μm film height, the simulation overestimates the measured compliance. A possible reason may be the assumption of an ideal bearing geometry, whose relative error is the largest at small film heights. The low coherence at a film thicknesses of 15 and 20 μm below 1 Hz is conspicuous. The suspected cause for this is the hydraulic pulsation of the supply, but this cannot be conclusively confirmed. A slight deviation is present for film thicknesses above 15 μm and frequencies greater than 1 kHz. Taking into account the experimental uncertainties, the measurements and simulation show excellent agreement and validate the developed model.

It is evident for all film heights that the test bench has a significant influence on the result of the simulation. The cause for this is the serial connection of the dynamic stiffness of the SR bearing and the static stiffness of the test bench (see Fig. 7). Because the stiffness and damping of the SR bearing depend solely on the film geometry and fluid properties, they are frequency independent and thus constant. However, due to the frequency independent damping constant, the dynamic stiffness increases with increasing excitation frequency. The test bench stiffness is also frequency independent and thus constant. As a result, at low frequencies, the dynamic bearing stiffness is significantly lower than the static stiffness of the test bench. Therefore, the dynamic behaviour of the SR bearing is dominant and the simulations with and without the test bench only differ marginally. At high frequencies, the stiffness ratio changes so that the dynamic behaviour of the test bench dominates the measurements and the simulation. Therefore, the compliance and the phase angle converge with increasing excitation frequency towards those of an oscillator with mass m and stiffness k_{TB}.

The simulation and measurement comparison of the shallow recess bearing compensated by a capillary (see Fig. 9) shows the measured and simulated dynamic compliance for the four film thicknesses. All measurements use the identical external restrictors designed for 20 μm film thickness. Therefore, the influence at shallow film thicknesses is almost negligible, whereas the impact increases with increasing film thickness.

The figure includes a simulation with and without the test bench extended with the effect of the uncertainties. Due to the introduced capillary, the bulk modulus and the external hydraulic resistance are no longer negligible. The two dominant uncertainties are now the bearing geometry and the bulk modulus. At low film height, where the influence of the capillary is negligible, the geometric uncertainty can explain the deviation between the measurement and the simulation. With the increasing influence of the capillary with the film height, the influence of the bulk modulus becomes the second dominant uncertainty.

The simulation and measurements show minimal deviation but are marginally higher than the SR without an external compensation device. The effect of low coherence is also present at 20 μm and below 1 Hz. A slight deviation is present for film thicknesses above 10 μm and frequencies greater than 1 kHz. Considering the experimental uncertainties, the measurements and the simulation show excellent agreement and validate the developed model.

Analogous to the measurements without an external compensation device (capillary), the dynamic behaviour of the test bench dominates the measured FRF at high frequencies, both the compliance and the phase angle.

4.3. Influence of the compressible volume on a shallow recess bearing compensated by a capillary

The damping of SR bearings only depends on the geometry of the bearing and the dynamic viscosity of the fluid. Therefore, it is not influenced by the compressible volume (see Appendix C). According to Eq. (8), the bearing stiffness corresponds to the ratio of the differentials of the bearing force and the film height. A change in film height affects the pressure profile, respectively, the bearing force, according to two different mechanisms:

- Change in the step pressure p_1 due to inherent control of SR bearings.
- Change in the pocket inlet pressure p_0 due to external capillary.

In the case of dynamic excitation, the inherent stiffness of the SR bearing remains constant, but the compressible volume reduces the influence of the capillary due to the decreasing bearing inlet pressure deviation Δp_0. According to 3.1.4, the dynamic pocket pressure is calculated based on the flow continuity equation. By rearranging Eq. (17), the relationship between pocket inlet pressure deviation and compressible volume becomes apparent:

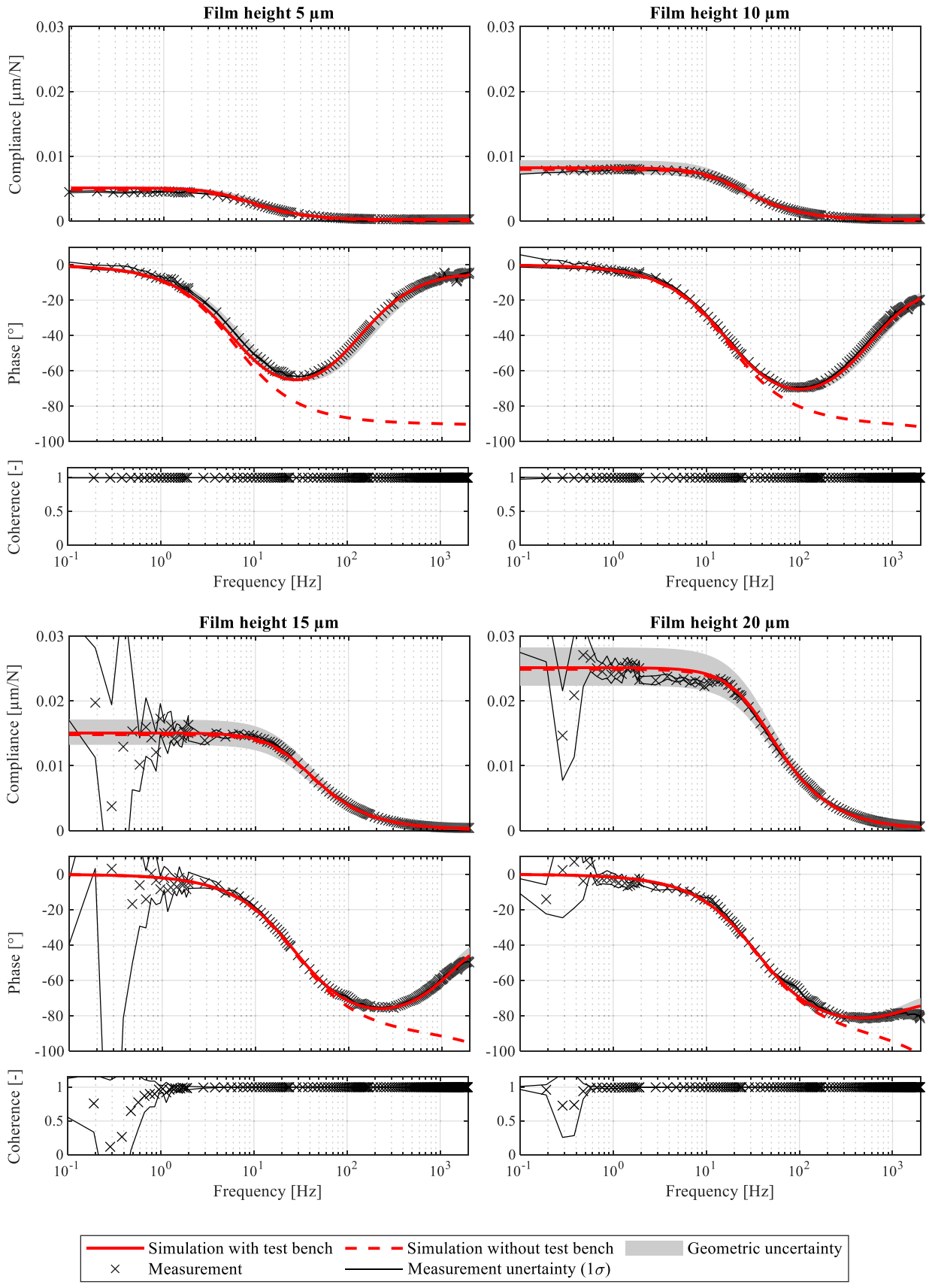

Fig. 8. Dynamic compliance - shallow recess bearing (without capillary).

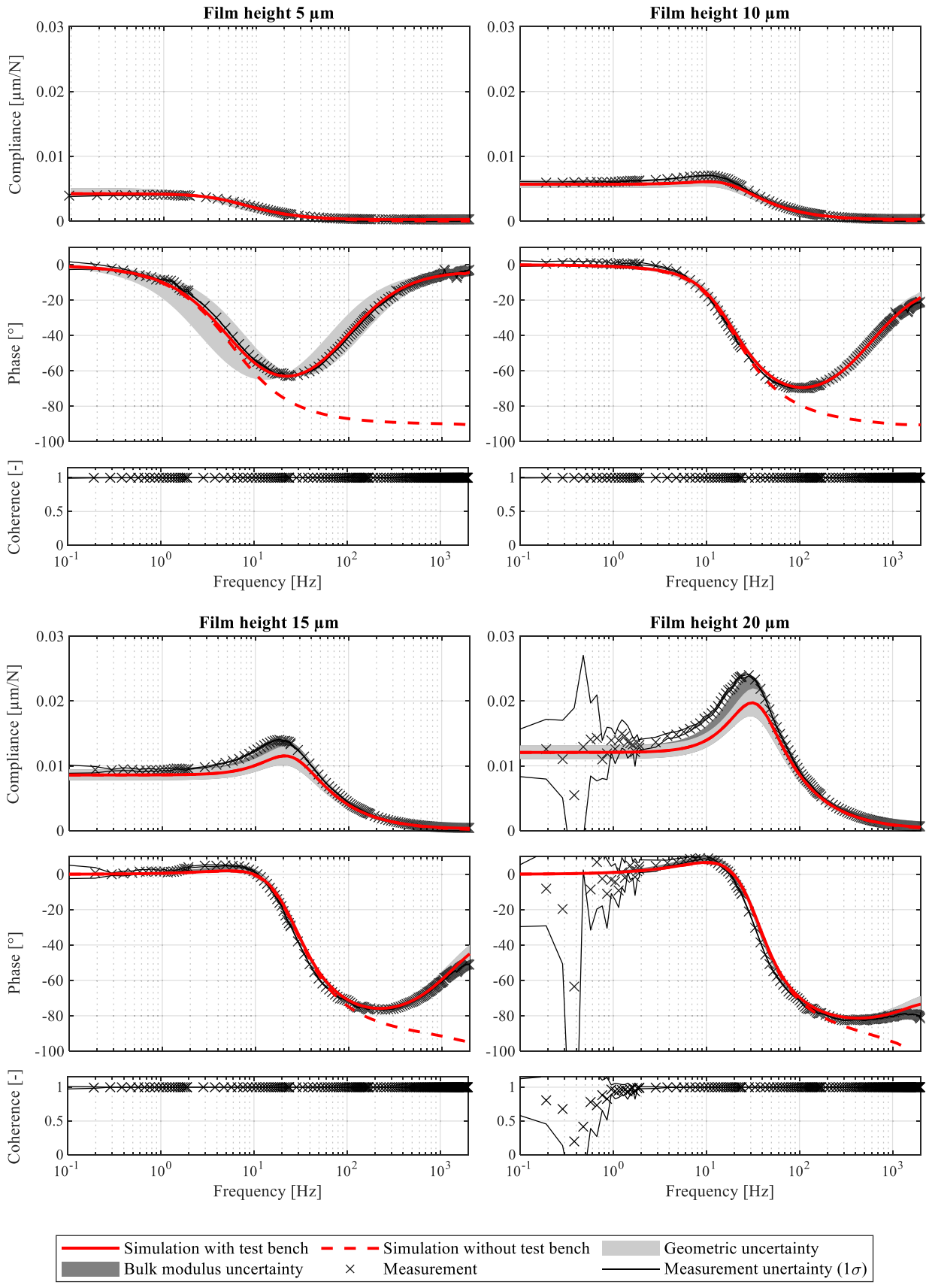

Fig. 9. Dynamic compliance - shallow recess bearing compensated by a capillary.

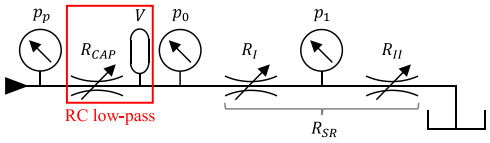

Fig. 10. Hydraulic schematics of SR HS bearing controlled by linear hydraulic resistance (capillary), including hydraulic capacity.

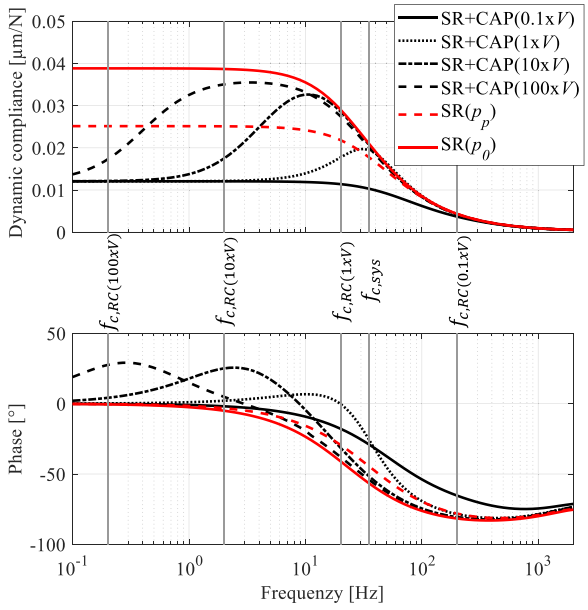

Fig. 11. Influence of compressible volume V on the dynamic compliance at 20 µm film thickness.

$$\Delta p_0(t) = \frac{K}{V}\int Q(t)dt \tag{25}$$

According to this equation, the pocket inlet pressure deviation is inversely proportional to the compressible volume. Thus, with increasing compressible volume and identical volume flow, the pressure change of the system decreases, i.e., the system response is damped. This effect also increases with the excitation frequency since the magnitude of the integral of the volume flow decreases with decreasing period. An extension of Fig. 6 by the compressible volume V leads to Fig. 10.

Analogous to electric circuits, the combination of a constant hydraulic resistance and a hydraulic capacity behaves as an RC low pass filter. Its cut-off frequency $f_{c,RC}$ can be calculated by:

$$f_{c,RC} = \frac{1}{2\pi \frac{R_{SR}R_{CAP}}{R_{SR}+R_{CAP}}C} \tag{26}$$

As the influence of the CAP increases with the film thickness, the following study deals with 20 µm film thickness. Fig. 11 shows a parameter study on the impact of the compressibility, varied by the compressible volume. Therefore, the actual compressible volume V is multiplied by 0.1, 1, 10 and 100. The corresponding cut-off frequency of the RC low pass filter for each volume and the cut-off frequency of the mechanical system $f_{c,sys}$ are marked for reference. In addition, the figure contains two graphs of SR bearings without external resistance for reference.

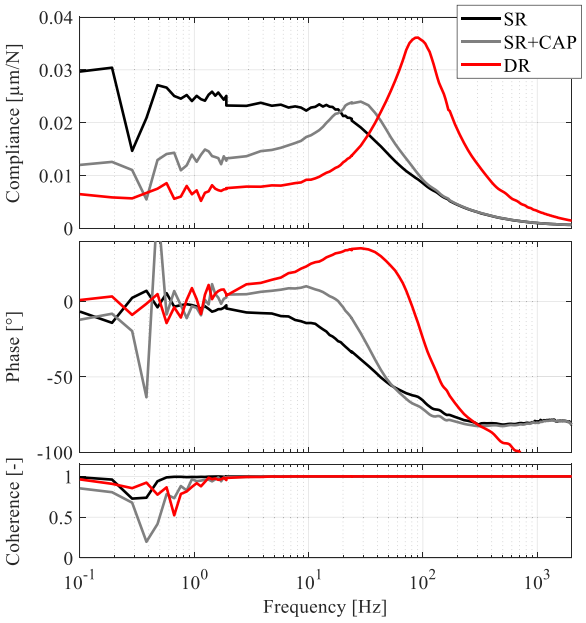

Fig. 12. Comparison of the measured FRF of a shallow recess bearing (SR), a shallow recess bearing with external capillary (SR+CAP) and a deep recess bearing with external capillary (DR) at a nominal film height of 20 µm.

Graph SR(p_0) represents a SR bearing without external resistance at the inlet pressure p_0 (see Eq. (10)). This estimates the worst case, whereby the external capillary only causes a constant pressure drop without contributing any stiffness. Graph SR(p_p) acts as a reference for the dynamic compliance if no external resistance is used and the SR bearing is supplied directly by the supply pressure.

As the volume increases, the frequency decreases, up to which the influence of the external resistance is present. Due to the inherent stiffness of SR bearings, the compliance is limited for a large volume and tends to an envelope graph that corresponds to SR(p_0). Therefore, the effect of an external restrictor depends significantly on the volume and compressibility between the restrictor and the bearing. Consequently, an external resistance does not necessarily lead to increased dynamic stiffness. For relatively large volumes, it can also have a negative effect. In this case, the capillary only reduces the supply pressure of the shallow recess bearing.

SR bearings without external controllers have constant compliance at low frequencies. When adding a capillary, a correlation between corner frequency of the supply system $f_{c,RC}$ and FRF of the bearing can be seen in this range, causing an increase in compliance. An approximate estimate of the influence of an additional capillary is possible by comparing the cut-off frequency of the hydraulic supply $f_{c,RC}$ to the cut-off frequency $f_{c,sys}$ of the mechanical system. For a global reduction in compliance, the following ratio serves as a reference:

$$f_{c,RC} > f_{c,sys} \tag{27}$$

If the cut-off frequency does not satisfy the requirement, the capillary lowers the dynamic stiffness for a specific frequency range compared to a standalone shallow recess bearing.

4.4. Comparison of experimental FRF of a shallow recess and a deep recess bearing

To classify the results presented, Fig. 12 compares the measured FRF of the SR bearing and the SR bearing + CAP from Fig. 8 and 9 with the FRF of a deep recess (DR) bearing at a film height of 20 μm. Appendix A contains the dimensions of the used deep recess pocket module and Appendix B lists the measured values of the experiment. When using the deep recess bearing, the compressible volume increases marginally due to the deep recess. To increase visibility, the individual measuring points are represented by their connecting lines and the measurement uncertainty representation is neglected.

The static compliance of the deep recess bearings is generally lower than that of the SR+CAP and SR bearings [9]. However, as the excitation frequency increases, this behaviour changes. Neglecting the measurements at low frequencies (< 2 Hz), the SR bearing shows a constant compliance of approximately 23 nm/N, which decreases from 16 Hz. In contrast, both bearings with external capillary first exhibit an increase in compliance before it reduces. The deep recess bearing exhibits the highest dynamic compliance (maximum: 36 nm/N at 91 Hz), whereas the SR+CAP bearing exhibits a lower increase (maximum: 24 nm/N at 29 Hz). This reduced increase is due to the inherent stiffness of the SR bearing, which limits the maximum compliance (see Section 4.3). Thus, SR+CAP bearings are more robust to the influence of hydraulic capacity than deep recess bearings. On the other hand, SR bearings (without capillary) are entirely independent of this issue.

5. Conclusion

State-of-the-art shallow recess bearing models refer only to static behaviour. This paper addresses the dynamic stiffness (compliance) of circular oil hydrostatic shallow recess thrust bearings theoretically and experimentally to expand the state of knowledge. The experiments validated the innovative theoretical models. Furthermore, an experimental comparison was made with a deep recess bearing using the identical test setup to classify the dynamic behaviour of SR bearings.

We provide:

- An analytical model of the static stiffness and damping of shallow recess thrust bearings.
- A Model of the dynamic behaviour of shallow recess thrust bearings with and without a capillary.
- A method to evaluate the benefit of using shallow recess bearings combined with a capillary.

For applications with periodic excitation with a wide range of frequencies, such as machine tools, there are high requirements for vibration elimination. However, using static parameters, predicting the system behaviour for such periodic loads is possible only to a limited extent. This paper provides a new approach to describe the dynamic behaviour of shallow recess thrust bearings. Especially in system design, a precise prediction of system behaviour is achievable.

An analysis of the results suggests the following:

- A spring and a damper in a parallel arrangement can represent a shallow recess pocket. Furthermore, the compressibility of the fluid is neglectable.
- Compressibility effects are no longer negligible for shallow recess pockets combined with an external capillary. The volume, respective, compressibility between the hydrostatic pocket and the capillary highly affects the dynamic compliance. Therefore, the stiffness of the spring is frequency-dependent, which introduces a phase shift. Thus, the model complexity increases. However, the capillary does not influence the squeeze damping, as it depends only on the bearing geometry and the fluid viscosity.
- Unlike deep recess pockets with external capillaries, for shallow recess pockets, no catastrophic failure occurs at high compressibility due to the inherent stiffness of shallow recess bearings.
- For infinitely high compressibility, the external capillary only lowers the inlet pressure of the shallow recess bearing and the overall compliance increases.
- The hydraulic supply system, consisting of hydraulic resistance and capacity, demonstrates a low pass filter behaviour. This circumstance influences the maximum frequency at which the assumption of a constant stiffness equal to the static stiffness is justifiable.
- The proposed computational model showed a high degree of agreement with the measurements.

The investigated film thicknesses range from 5 to 20 μm at a constant supply pressure of 10.5 MPa. The excitation signal ranges from 0.1 to 2000 Hz.

Appendix A.) Engineering drawings of the bearing components

See Fig. A1 and Fig. A2.

Funding

The work was supported by the Grant Agency of the Czech Technical University in Prague, grant no. SGS22/159/OHK2/3 T/12 provided material support for the experiments.

CRediT authorship contribution statement

F. A. Tripkewitz: Supervision, Project administration, Conceptualization, Methodology, Software, Visualization, Writing – original draft. **T. Lazák:** Conceptualization, Methodology, Software, Visualization, Investigation, Writing – original draft. **M. Fritz:** Conceptualization, Resources, Writing – review & editing. **E. Stach:** Writing – Reviewing & Editing. **M. Weigold:** Writing – review & editing. **M. Sulitka:** Resources, Writing – review & editing.

Declaration of Competing Interest

The authors declare that they have no known competing financial interests or personal relationships that could have appeared to influence the work reported in this paper.

Data Availability

Data will be made available on request.

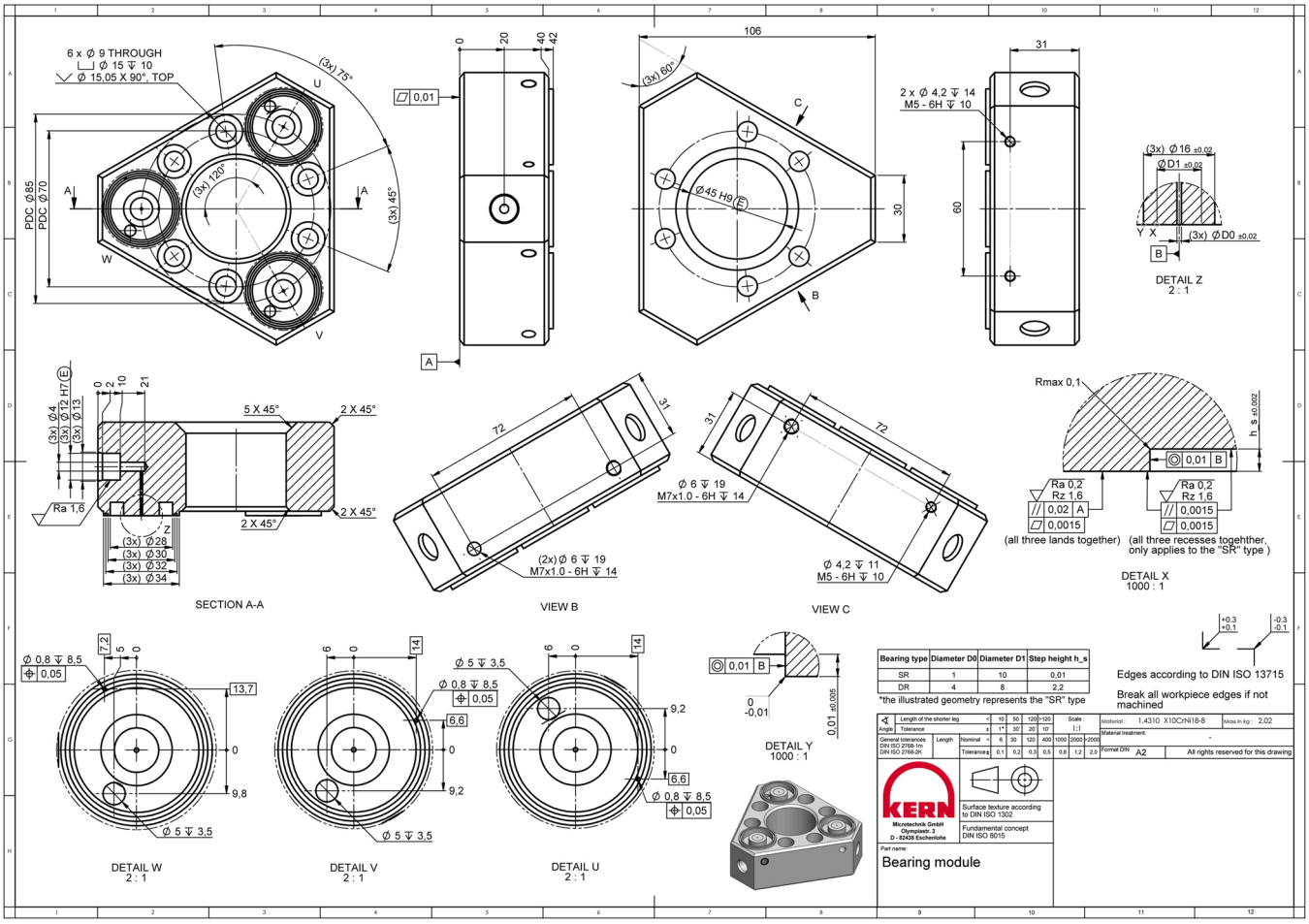

Fig. A1. Engineering drawing of the pocket modules (Details X, Y and Z show the bearing geometry).

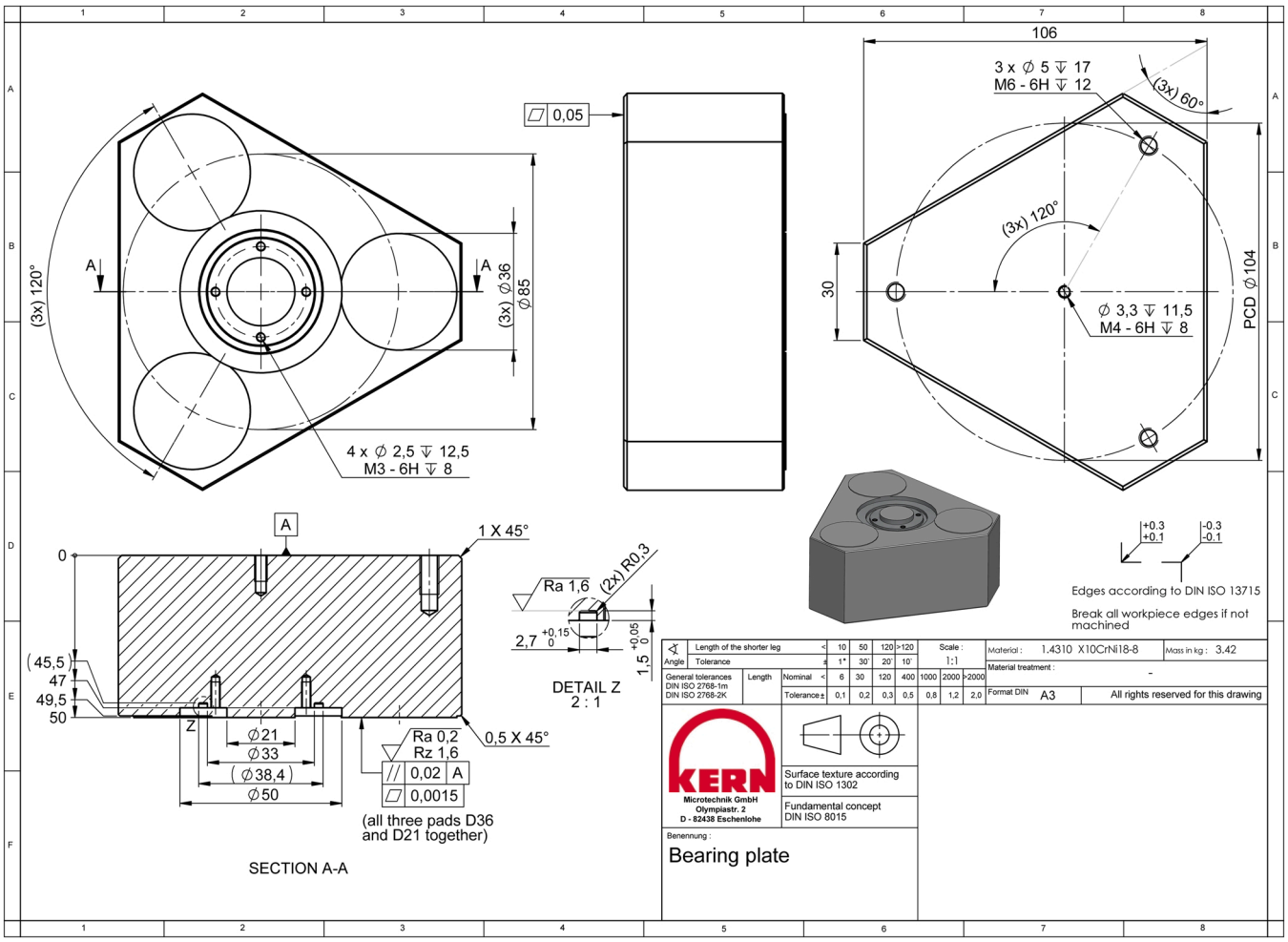

Fig. A2. Engineering drawing of the bearing plate.

Appendix B.) Table of values measured in the experiments

See Table B1 and Table B2.

Table B1
Values measured in the experiments with the shallow recess bearing module.

External compensation device	Nominal film thickness [μm]	Measured film thickness [μm]	Supply pressure [MPa]	Preloading force [N]	Fluid Temperature T_0 [°C]
No	5	4.9	10.57	3279	21.47
No	10	10.0	10.56	2406	22.86
No	15	15.0	10.52	1944	24.24
No	20	19.9	10.47	1725	24.99
Yes	5	4.1	10.55	3442	23.00
Yes	10	10.0	10.54	2152	23.54
Yes	15	15.0	10.51	1470	24.16
Yes	20	19.8	10.48	1055	24.87

Table B2
Values measured in the experiments with the deep recess bearing module.

External compensation device	Nominal film thickness [μm]	Measured film thickness [μm]	Supply pressure [MPa]	Preloading force [N]	Fluid Temperature T_0 [°C]
Yes	20	19.8	10.49	1649	23.2

Appendix C.) Derivation of damping constant for shallow recess bearings

Integration of (15) leads to:

$$r\frac{\partial p}{\partial r} = -\frac{12\mu}{h^3}\frac{r^2}{2}\frac{\partial h}{\partial t} + c_1 \tag{C.1}$$

The equation is then divided by r and integrated with respect to r.

$$p = -\frac{6\mu}{h^3}\frac{r^2}{2}\frac{\partial h}{\partial t} + c_1\ln(r) + c_2 \tag{C.2}$$

Equation (C.2) describes the pressure distribution in both sections of the HS bearing. Only the integration constants differ in each area. In the following, the superscript index I represents the recess and the superscript index II represents the land. The integration constants for both sections are derived from the following four boundary conditions:

1) The pressure at the inlet of the shallow recess is equal to zero ($p(r_0) = 0$). Further, $\sigma_2 = 6\mu\frac{\partial h}{\partial t}$ is substituted into (C.2).

$$0 = -\frac{\sigma_2}{h_I^3}\frac{r_0^2}{2} + c_1^I\ln(r_0) + c_2^I \tag{C.3}$$

2) The pressure at the outlet of the land is also equal to zero ($p(r_2) = 0$).

$$0 = -\frac{\sigma_2}{h_{II}^3}\frac{r_2^2}{2} + c_1^{II}\ln(r_2) + c_2^{II} \tag{C.4}$$

3) Pressure at the step ($r = r_1$) is equal for both areas.

$$-\frac{\sigma_2}{h_I^3}\frac{r_1^2}{2} + c_1^I\ln(r_1) + c_2^I = -\frac{\sigma_2}{h_{II}^3}\frac{r_1^2}{2} + c_1^{II}\ln(r_1) + c_2^{II} \tag{C.5}$$

4) The last condition addresses the pressure gradient at the step for both areas. The condition is obtained by integrating (15) over an infinitely small region around the step from the left side and the right side. (Here, the film thickness h changes with radius r) Thus,

$$rh_{II}^3\frac{\partial p}{\partial r}\Big|_{r_+} = rh_I^3\frac{\partial p}{\partial r}\Big|_{r_-} \tag{C.6}$$

$r\frac{\partial p}{\partial r}$ is substituted from (C.1) and thus

$$c_1^{II}h_I^3 - c_1^I h_I^3 = 0 \tag{C.7}$$

The integration of pressure in the recess and land areas leads to the corresponding squeeze forces.

$$F_{sq,I} = \int_{A_I} p_I dA = \int_{r_0}^{r_1} 2\pi r p_I dr \tag{C.8}$$

$$F_{sq,II} = \int_{A_{II}} p_{II} dA = \int_{r_1}^{r_2} 2\pi r p_{II} dr \tag{C.9}$$

Squeeze damping force F_d equals the sum of force (C.8) and (C.9). Squeeze damping corresponds to the quotient of damping force relative velocity of the bearing surfaces (see Fig. 4, components A and B).

$$d_{SR} = \frac{d_{num}}{d_{den}} = -\frac{F_d}{w} \tag{C.10}$$

The equations for the numerator and denominator of the squeeze damping d_{SR} are:

$$\begin{aligned} d_{num} = 6\pi\mu(&h_I{}^6r_1{}^4 + h_{II}{}^6r_0{}^4 + h_I{}^6r_2{}^4 + h_{II}{}^6r_1{}^4 - 2h_I{}^3h_{II}{}^3r_1{}^4 - 2h_{II}{}^6r_0{}^2r_1{}^2 - 2h_I{}^6r_1{}^2r_2{}^2 - h_{II}{}^6r_0{}^4\ln(r_0) - h_I{}^6r_1{}^4\ln(r_1) + h_{II}{}^6r_0{}^4\ln(r_1) + h_{II}{}^6r_1{}^4\ln(r_0) + h_I{}^6r_1{}^4\ln(r_2) \\ &+ h_I{}^6r_2{}^4\ln(r_1) - h_{II}{}^6r_1{}^4\ln(r_1) - h_I{}^6r_2{}^4\ln(r_2) + 2h_I{}^3h_{II}{}^3r_0{}^2r_1{}^2 - 2h_I{}^3h_{II}{}^3r_0{}^2r_2{}^2 + 2h_I{}^3h_{II}{}^3r_1{}^2r_2{}^2 - h_I{}^3h_{II}{}^3r_0{}^4\ln(r_1) - h_I{}^3h_{II}{}^3r_1{}^4\ln(r_0) + h_I{}^3h_{II}{}^3r_0{}^4\ln(r_2) \\ &+ 2h_I{}^3h_{II}{}^3r_1{}^4\ln(r_1) + h_I{}^3h_{II}{}^3r_2{}^4\ln(r_0) - h_I{}^3h_{II}{}^3r_1{}^4\ln(r_2) - h_I{}^3h_{II}{}^3r_2{}^4\ln(r_1)) \end{aligned} \tag{C.11}$$

$$d_{den} = 4h_I{}^3h_{II}{}^3(h_I{}^3\ln(r_1) + h_{II}{}^3\ln(r_0) - h_I{}^3\ln(r_2) - h_{II}{}^3\ln(r_1)) \tag{C.12}$$

References

[1] Slocum A, Marsh ER, Smith DH. A new damper design for machine tool structures: the replicated internal viscous damper. Precis Eng 1994:174–83. https://doi.org/10.1016/0141-6359(94)90122-8.

[2] Schellekens P, Rosielle N, Vermeulen H, Vermeulen M, Wetzels S, Pril W. Design for precision: current status and trends. CIRP Ann 1998:557–86. https://doi.org/10.1016/S0007-8506(07)63243-0.

[3] Bassani R, Piccigallo B. Hydrostatic Lubrication. Amsterdam: Elsevier Science; 1992.

[4] Winterschladen M. Verfahren zur ganzheitlichen Auslegung von hydrostatischen Führungen und Lagern. Aachen: Shaker Verlag; 2008.

[5] Rowe WB. Dynamic and static properties of recessed hydrostatic journal bearings by small displacement analysis. J Lubr Technol 1980:71–9. https://doi.org/10.1115/1.3251441.

[6] San Andres L. Effects of fluid compressibility on the dynamic response of hydrostatic journal bearings. WEAR 1991:269–83. https://doi.org/10.1016/0043-1648(91)90068-6.

[7] Adams CR. The step bearing - a new concept in air lubrication. Prod Eng 1958:96–9.

[8] Adams CR, Dworski J, Shoemaker EM. Externally pressurized step journal bearings. J Basic Eng 1961:595–602. https://doi.org/10.1115/1.3662276.

[9] O'Donoghue JP, Hooke CJ. Design of inherently stable hydrostatic bearings. Proc Inst Mech Eng 1968:172–6.

[10] Hale LC, Donaldson RR, Castro C, Chung HDJ. Development of a hydrostatic journal bearing with slit-step compensation. Am Scociety Precis Eng - Annu Meet 2006.

[11] Tripkewitz FA, Fritz M, Weigold M. Experimental study on the tilting stiffness of oil hydrostatic shallow recess thrust bearings. MM Sci J 2021. https://doi.org/10.17973/MMSJ.2021_11_2021141.

[12] Rowe WB. Hydrostatic, Aerostatic and Hybrid Bearing Design. Elsevier Butterworth Heinemann; 2013. https://doi.org/10.1016/C2011-0-07331-3.

[13] Karjalainen JP, Karjalainen R, Huhtala K. Measuring and modelling hydraulic fluid dynamics at high pressure—accurate and simple approach. Int J Fluid Power 2012:51–9. https://doi.org/10.1080/14399776.2012.10781053.

[14] Schroeder M. Synthesis of low-peak-factor signals and binary sequences with low autocorrelation (Corresp.). IEEE Trans Inf Theory 1970:85–9. https://doi.org/10.1109/TIT.1970.1054411.

[15] Herlufsen H. Dual channel FFT analysis (Part I). Brüel & Kjær,; 1984.

[16] Brown GM. The dynamic characteristic of a hydrostatic thrust bearing. Int J Mach Tool Des Res 1961:157–71. https://doi.org/10.1016/0020-7357(61)90050-6.

[17] Cameron A. The principles of lubrication. London: Longmas; 1966. p. 591.